Supplementary Material: Roughness on liquid-infused surfaces induced by capillary waves

Johan Sundin[1], Stéphane Zaleski[2,3] and Shervin Bagheri[1]
[1]*Linné FLOW Centre, Dept. Engineering Mechanics, KTH, Stockholm, Sweden*
[2]*Sorbonne Université & CNRS, Institut Jean Le Rond d'Alembert, UMR 7190, Paris, France*
[3]*Institut Universitaire de France, Institut Jean Le Rond d'Alembert, UMR 7190, Paris, France*

S1. DETAILS OF NUMERICAL METHODS

In this section, we describe the schemes of the numerical code that was used to solve the two-component flow over and inside the textured surfaces. For momentum convection, a second-order central scheme was used, whereas a third-order Runge-Kutta scheme was used for time integration [1]. The equation for the pressure was solved with a fast Fourier transform (FFT) solver (FFTW) and handling domain decomposition with the 2DECOMP&FFT library. To describe solids, we used a grid-aligned immersed-boundary method (IBM) [2]. With this method, the edge of the solid is located at the edge of the cells. For a staggered grid, this means that the top of the solid ridges are at the location of the wall-normal velocity nodes.

To impose a contact angle at the liquid-liquid-solid contact line, we specified the height function of the first ghost layer [3]. Since the IBM is grid-aligned, the implementation of the contact angle is the same on an the immersed boundaries and the domain boundaries. We used a dynamic model of the contact angle based on hydrodynamic theory [4] – adapted to VOF [5] – , together with a no-slip velocity condition. As shown in [5], the dynamic contact angle also improves grid independence. The method is explained further in sec. S1 A. It should be noted that the ridge corners' ghost cells were set to always be interface cells, and that the contact angle was imposed when the interface moved to adjacent cells. Depinning occured for the higher Weber numbers.

The turbulent flow was validated by comparing the mean flow and the r.m.s. velocities for a full channel with smooth walls to data from ref. [6]. The results are shown in fig. S1, having for the mean velocity a deviation of 0.8% at the channel center. Shown are also statistics of a smooth open channel, with only small deviations for $y^+ < 100$.

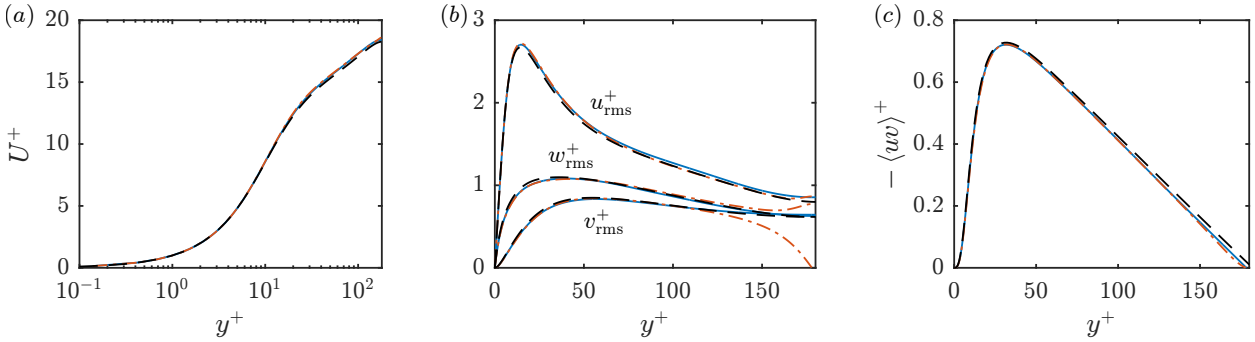

FIG. S1: Simulation of a turbulent channel flow with smooth walls at $\mathrm{Re}_\tau \approx 180$, with mean velocity ($a$), r.m.s. velocities ($b$), and Reynolds shear stress (c). The spanwise velocity r.m.s. value is represented by w^+_{rms} for convenience, but elsewhere w refers to the groove width. —— PARIS; — · — PARIS open channel; — — — Lee & Moser (2015) [6]

The description of the streamwise liquid filled grooves was validated against the analytical expressions of Schönecker et al. [7] for the slip length in a laminar flow. These expressions have recently also been used as a reference for turbulent data of LIS simulations [8]. For these tests, we use a computational box corresponding to a unit cell of the surface, with height three times the height of the groove. On the top boundary, a constant shear was applied in the streamwise direction. A similar setup was recently used to investigate the robustness of LIS with spanwise grooves [9]. Having 50 cells in the grooves, the errors were less than 4% for $\mu_i/\mu_\infty = 0.5, 1$ and 2, see fig. S2.

A grid refinement study was also performed for $\mu_i/\mu_\infty = 1$, $\mathrm{We} = 100$ and $\theta = 45°$, where another grid with $(N_x, N_y, N_z) = (384, 960, 1536)$ was used, increasing the total number of grid cells by a factor of 3.4. This gave a change of the friction coefficient by 0.76%. Plots are shown in fig. S3.

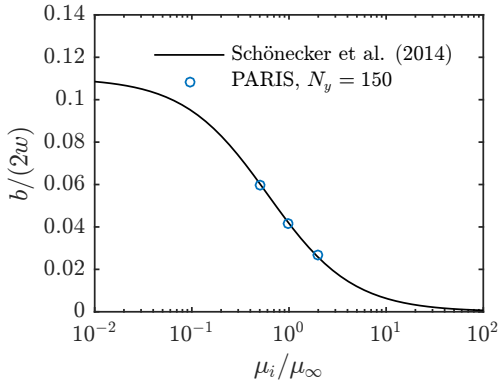

FIG. S2: Comparison of slip length with the expressions of Schönecker *et al.* (2014). N_y refers to the total number of grid cells in the wall-normal direction, with $N_y/3 = 50$ in the groove.

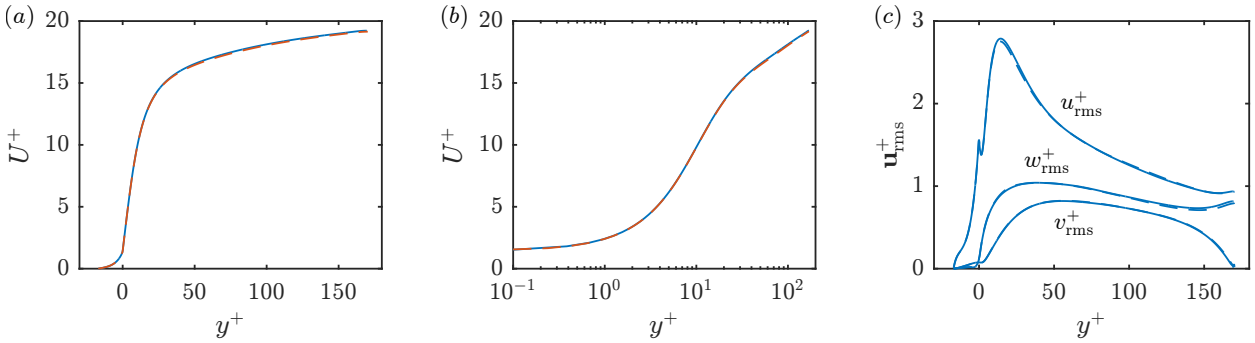

FIG. S3: Grid refinement study: —— regular grid; — — — refined grid. The spanwise velocity r.m.s. value is represented by w^+_{rms} for convenience.

A. Dynamic contact angle

Following ref. [5], the contact angle can be found from the equation

$$G^*(\theta_{\mathrm{num}}) = G^*(\theta_{\mathrm{stat}}) + \mathrm{Ca}\ln\left(\frac{\Delta/2}{\lambda}\right), \tag{S1}$$

where θ_{num} is the numerically imposed contact angle, θ_{stat} is the static angle, $\mathrm{Ca} = U_{\mathrm{cl}}\sqrt{\mu_i\mu_\infty}/\gamma$, with contact line velocity U_{cl}, λ is a microscopic length scale corresponding to an effective slip length of the contact line, here taken to be constant, and Δ is the wall-normal cell height. The angle θ_{stat} is in this manuscript denoted only θ for simplicity. The contact line velocity is measured half a cell above the wall. The function $G^*(\theta)$ is a monotonically increasing function. It is defined as $G^*(\theta) = \sqrt{q}G(\theta)$, where $q = \mu_\infty/\mu_i$ and $G(\theta)$ is the original function derived by ref. [10], with the extra factor for increased symmetry,

$$G^*(\theta) = \int_0^\theta f^{*-1}(\theta', q)\mathrm{d}\theta', \tag{S2}$$

with

$$f^{*-1}(\theta, q) = \frac{q^{0.5}(\theta^2 - \sin^2\theta)[(\pi-\theta) + \sin\theta\cos\theta] + q^{-0.5}((\pi-\theta)^2 - \sin^2\theta)[\theta - \sin\theta\cos\theta]}{2\sin\theta[(2-q-q^{-1})\sin^2\theta + q\theta^2 + q^{-1}(\pi-\theta)^2 + 2\theta(\pi-\theta)]}. \tag{S3}$$

When written in this form, it is apparent that $f^*(\theta, q) = f^*(\pi - \theta, q^{-1})$, which is a necessary requirement, since eq. (S1) should be independent of which of the two components we consider. This is identical to the hydrodynamic theory of an apparent angle model suggested in ref. [10], where θ_{num} is the apparent angle. Legendre and Maglio [5]

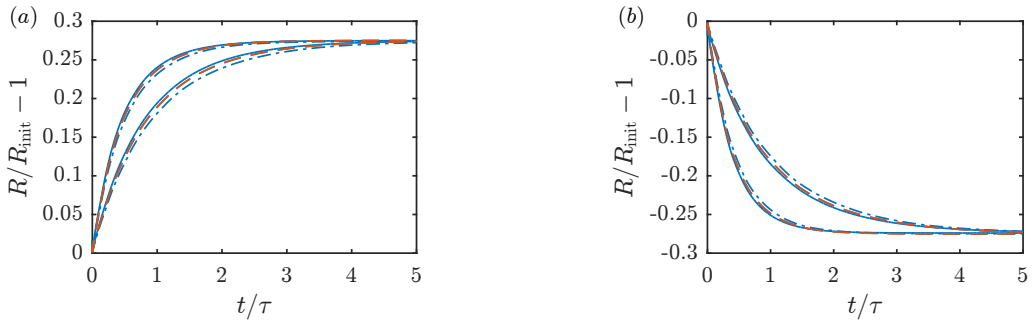

FIG. S4: Radius at wall ($y = 0$) of droplet spreading from 90° to 60° (a), and contracting from 90° to 120° (b), for three different wall-normal cell sizes: —— $N_y = 32$; — — — $N_y = 64$; — · — $N_y = 128$, in blue. The viscosity ratios are 0.5 and 2, with the faster spread/contraction for the case with surrounding fluid of lower viscosity. Data from a droplet on an immersed boundary are also shown, using the intermediate resolution (red, — — —).

has suggested that λ should be on the order of the the physical slip length (typically on the order of 1 nm), and may or may not be used in combination with a numerically applied slip length. We use a no-slip condition, with a numerical value of $\lambda = 2 \cdot 10^{-7} h$, that with $h \approx 0.5$ cm attains a realistic value. The full equation (S1) was solved by the Newton's method, and $f^{*-1}(\theta, N)$ was integrated with the trapezoidal rule. For numerical reasons, the value has been limited to $30° \leq \theta_{\text{num}} \leq 150°$.

We evaluated the grid-independence of the contact line model by looking at droplet spreading for three different cell sizes. A three dimensional half-sphere droplet of radius $R_{\text{init}} = 0.5$ was placed in a box of size $(L_x, L_y, L_z) = (2, 1, 2)$, with periodic boundary conditions in the x- and z-directions, and no-slip and shear-free boundary conditions in the negative and positive y-direction, respectively. The initial radius sets the length scale of the problem. The contact angle was initially 90°, when the static contact was set to $\theta_{\text{stat}} = 60°$, so that the droplet started to spread. The droplet had a density $\rho = 1$, viscosity $\mu = 0.25$ and surface tension $\gamma = 7.5$. Using the density and the viscosity we can define a time scale $\tau = \rho R_{\text{init}}^2 / \mu$. The surrounding fluid had the same density, and the viscosity ratio was changed by varying the viscosity of the surrounding fluid. Viscosity ratios of both 0.5 and 2 were tested, to span the range of this study. The number of cells of the wall parallel directions were $N_x = 64$ and $N_z = 64$, and the number of cells of the wall-normal direction was varied between $N_y = 32$, $N_y = 64$ and $N_y = 128$. The microscopic length scale was set to $\lambda = 2 \cdot 10^{-7}$. Resulting spreading radii are shown in fig. S4a. The differences between the curves are a few percentage, considered small enough for this study. Corresponding droplet contraction tests, with contraction from 90° to 120°, are shown in fig. S4b. The tests using the intermediate resolution were also repeated on an immersed boundary by extending the domain in the y-direction below the droplet by $\Delta L_y = 0.5$ and adding a solid slab there. The curves are hardly distinguishable between the two setups, as shown in fig. S4. The fluid parameters and the dynamic contact angle model are the same as those used by Legendre & Maglio [5] (Dyn2) for the spreading case, except for the viscosity ratio (there equal to 1) and a slightly different value of λ. Their results agree well with those shown here.

S2. TURBULENCE STATISTICS

In this section, we show the turbulent statistics corresponding to the simulations We $= \{100, 150, 200\}$ and viscosity ratios $\mu_i/\mu_\infty = \{0.5, 1, 2\}$. Mean velocity profiles are plotted in fig. S5a in wall units and fig. S5b in outer units. As can be seen from the plot in wall units, the centerline velocity is increased by the LIS for low We. This is related to the drag reduction achieved at these We, whereas the opposite occurs for the cases of drag increase [11]. A reduction of the centerline velocity is followed by a decrease in the streamwise r.m.s. component, and an increase of the wall-normal and the spanwise fluctuations, shown in fig. S5c. Over all, drag increase results in an increased isotropy of the velocity fluctuations. Increased wall-normal velocity fluctuations at the surface has a strong connection to the increase in drag [12, 13]. It implies stronger flow ejections, caused by the roughness the waves impose.

The pressure r.m.s. profiles are shown in fig. S5d. Outside the grooves, the profiles for We = 100 and We = 150 are similar to the smooth wall profile, but are higher inside the grooves. For We = 200, when there are large waves, the pressure fluctuations are increased also outside the grooves. This could be due to the increased roughness, but also due to formation of droplets.

In the streamwise r.m.s. component, fig. S5c, there is a peak at $y = 0$, but not for the spanwise nor for the

wall-normal. This can be related to the dispersive stresses from the solid structures, which are the r.m.s. of the roughness-coherent velocity, $\mathbf{u}_{\mathrm{RC}}$. Due to the symmetry in the streamwise direction, the roughness-coherent velocity is the velocity field averaged in the streamwise direction and time. A peak is then created because the streamwise velocity component on average is larger over the interface at the grooves than over the ridges. The peak height differs between the viscosity ratios, but not so much between the different Weber numbers. This reflects the behaviour of the mean velocity at the interface, fig. S5a for small y^+, as well as the slip length, fig. 3b. It was seen that both the spanwise and wall-normal roughness-coherent components were close to zero. The streamwise part is shown in fig. S6 for We = 100.

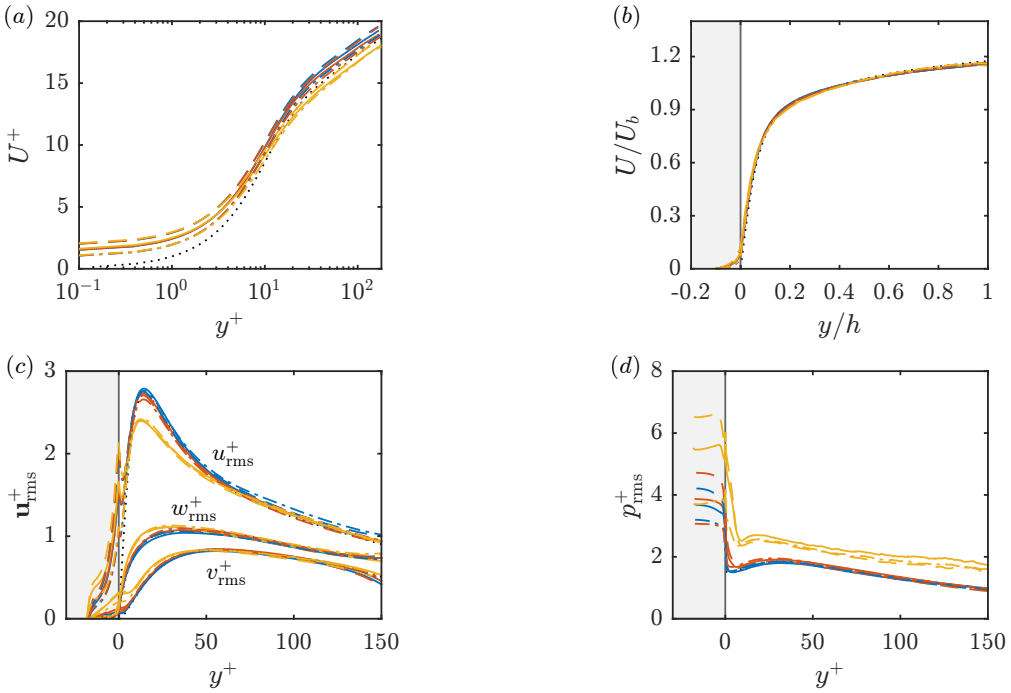

FIG. S5: Mean velocity profiles in wall units (a), and outer units (b) together with r.m.s. velocities (c) and r.m.s. pressure (d). The grey area represent the grooves. Colours represent different We as in fig. 3 (We = 100-blue, We = 150-red and We = 200-yellow), and the different lines represent different viscosity ratios, $\mu_i/\mu_\infty = 0.5$ (— — —), $\mu_i/\mu_\infty = 1$ (——) and $\mu_i/\mu_\infty = 2$ (— · —). Also shown are statistics for a smooth wall (· · · · · ·). The spanwise velocity r.m.s. value is represented by w^+_{rms} for convenience, but elsewhere w refers to the groove width.

.

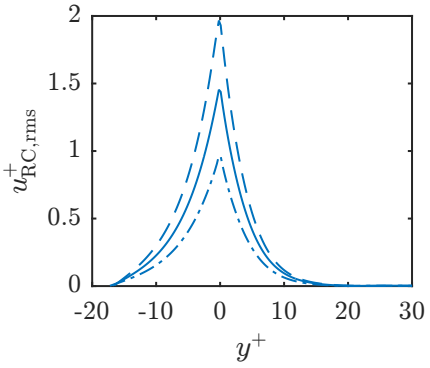

FIG. S6: Streamwise dispersive stress for We = 100, $\theta = 45°$ and $\mu_i/\mu_\infty = 0.5$ (— — —), $\mu_i/\mu_\infty = 1$ (——) and $\mu_i/\mu_\infty = 2$ (— · —).

S3. THE MILES INSTABILITY ON GROOVES

A. Governing equations

In this section, we look at the governing equations for the Miles instability. We start from the equations for a infinitesimal disturbance on a baseflow $U = U(y)$ [14],

$$\frac{\partial u}{\partial t} + U\frac{\partial u}{\partial x} + vU' = -\frac{1}{\rho}\frac{\partial p}{\partial x}, \tag{S4}$$

$$\frac{\partial v}{\partial t} + U\frac{\partial v}{\partial x} = -\frac{1}{\rho}\frac{\partial p}{\partial y}, \tag{S5}$$

$$\frac{\partial w}{\partial t} + U\frac{\partial w}{\partial x} = -\frac{1}{\rho}\frac{\partial p}{\partial z}, \tag{S6}$$

and

$$\frac{\partial u}{\partial x} + \frac{\partial v}{\partial y} + \frac{\partial w}{\partial z} = 0, \tag{S7}$$

where $'$ denotes a derivative in the y-direction. The spanwise velocity component is here represented by w for convenience, which elsewhere refer to the groove width. Eliminating p gives Rayleigh's equation for v (inviscid Orr-Sommerfeld equation),

$$\left[\left(\frac{\partial}{\partial t} + U\frac{\partial}{\partial x}\right)\nabla^2 - U''\frac{\partial}{\partial x}\right]v = 0, \tag{S8}$$

with p given by

$$\frac{1}{\rho}\left[\frac{\partial^2}{\partial x^2} + \frac{\partial^2}{\partial z^2}\right]p = \frac{\partial^2 v}{\partial t \partial y} + U\frac{\partial^2 v}{\partial x \partial y} - U'\frac{\partial v}{\partial x}. \tag{S9}$$

We further assume an interface shape of a wave travelling in the streamwise direction,

$$\eta = Ae^{ik_x(x-ct)}\cos(k_z z) = Ae^{k_x c_i t}e^{ik_x(x-c_r t)}\cos(k_z z) = a(t)e^{ik_x(x-c_r t)}\cos(k_z z), \tag{S10}$$

where η is the location of the interface, A is the wave amplitude, k_x is the streamwise wavenumber, k_z is the spanwise wavenumber and $c = c_r + ic_i$. Henceforth, we'll use the notation $k = \sqrt{k_x^2 + k_z^2}$. The curvature of the interface gives rise to a pressure difference over the surface of (going from negative to positive y),

$$\Delta p_{\text{cap}} = \gamma\left(\frac{\partial^2}{\partial x^2} + \frac{\partial^2}{\partial z^2}\right)\eta = -\gamma k^2 \eta. \tag{S11}$$

The perturbation must die out at infinity,

$$v \to 0 \quad \text{as} \quad y \to \infty. \tag{S12}$$

In addition to this, fluid parcels on the interface must remain on the interface, (so that the interface remains a streamline) [15],

$$\frac{\partial \eta}{\partial t} + U\frac{\partial \eta}{\partial x} = v \implies \frac{v}{U-c} = ik_x\eta \quad \text{on } y = \eta \approx 0. \tag{S13}$$

Returning now to Rayleigh's equation, eq. (S8), with (x, z, t)-dependence of v as η,

$$(U-c)\frac{\partial^2 v}{\partial y^2} - [k^2(U-c) + U'']v = 0. \tag{S14}$$

From eq. (S9), with (x, z, t)-dependence of p as η,

$$\frac{p}{\rho} = -i\frac{k_x}{k^2}\left[(U-c)\frac{\partial v}{\partial y} - U'v\right]. \tag{S15}$$

B. Non-dimensionalisation

In order to facilitate the derivations, we introduce the transform,

$$\xi = ky, \quad U - c = U_1\tilde{u}(\xi) \quad \text{and} \quad v = ik_x U_1 \tilde{v}(\xi)\eta, \tag{S16}$$

where U_1 is an arbitrary reference velocity. From the kinematics of the interface, eq. (S13), it follows that

$$\tilde{v}_0 = \tilde{u}_0, \tag{S17}$$

where a subscript 0 denote the location of the interface, $y \approx 0$. The Rayleigh equation becomes

$$\tilde{v}''\tilde{u} - [\tilde{u} + \tilde{u}'']\tilde{v} = 0. \tag{S18}$$

The equation for the pressure, eq. (S15), results in

$$p = \rho U_1^2 \frac{k_x^2}{k}\eta(\tilde{u}\tilde{v}' - \tilde{u}'\tilde{v}). \tag{S19}$$

The pressure just above the interface can be written as

$$p_0^+ = (\alpha + i\beta)\rho U_1^2 \frac{k_x^2}{k}\eta. \tag{S20}$$

By comparing these two expressions,

$$\alpha + i\beta = (\tilde{u}_0\tilde{v}_0' - \tilde{u}_0'\tilde{v}_0) = \tilde{u}_0\left(\tilde{v}_0' - \tilde{u}_0'\right), \tag{S21}$$

where the last equality comes from eq. (S17). Following ref. [16], $\tilde{u}$ is assumed to be approximately real and thus β must come from the imaginary part of $\tilde{u}_0\tilde{v}_0'$, whereas α is the remaining part.

C. Derivation of α

We here derive an expression for α, which is the real part of eq. (S21),

$$\alpha = \Re(\tilde{u}_0\tilde{v}_0') - \tilde{u}_0\tilde{u}_0'. \tag{S22}$$

We use an approximate solution suggested by Miles [16], $\tilde{v} = \tilde{u}(\xi)e^{-\xi}$ (satisfying the boundary conditions), instead of solving the full equation. This approximate solution gives

$$\alpha = -\tilde{u}_0^2 - \tilde{u}_0\tilde{u}_0' = \frac{1}{U_1^2}\left(-(U_0 - c)^2 - \frac{U_0'}{k}(U_0 - c)\right). \tag{S23}$$

Now, α can be decomposed into two parts, $\alpha = \alpha_1 + \alpha_2$, where $\alpha_1 = -c^2/U_1^2$ and α_2 is the remaining part. We assume that U_0 can be neglected in comparison to c. The inverse of the wave number has an upper bound,

$$\frac{1}{k} = \frac{1}{\sqrt{k_x^2 + k_z^2}} < \frac{1}{k_z} = \frac{\lambda_z}{2\pi} < \frac{2w}{2\pi}, \tag{S24}$$

since $k_x > 0$ and λ_z must be smaller than two groove widths. Therefore,

$$\frac{U_0'}{k} = \frac{1}{kh}\frac{\mathrm{Re}_\tau^2}{\mathrm{Re}_b}U_b = \frac{11}{kh}U_b < \frac{11}{\pi}\frac{w}{h}U_b, \tag{S25}$$

for $\mathrm{Re}_\tau = 180$. For this Reynolds number and groove width $w^+ = 18$, the limiting value is 5.5 in wall units. The shear could hence potentially influence the phase speed with up to this magnitude, however we consider it here to be of secondary importance.

We now look at the flow inside the groove. The wall-normal velocity must be zero at the bottom at the groove,

$$\tilde{v} = 0 \quad \text{at} \quad \xi = -kw. \tag{S26}$$

It can also be noticed that $kw > k_z w \leq 2\pi/(2w)w = \pi$, and $e^{-\pi} = 0.043 \ll 1$. Hence, if the same assumption of exponential decrease of $\tilde{v}$ is made inside the groove, it is reasonable. We therefore assume $\tilde{v} = \tilde{u}e^{\xi}$ for $y < 0$. Neglecting also the mean velocity and its derivative inside the groove, the pressure is

$$p^- = \rho\frac{k_x^2}{k}c^2\eta e^{ky}, \quad y < 0, \tag{S27}$$

as given by eq. (S9) or eq. (S19). This is the pressure corresponding to α_1.

D. Phase speed and minimum phase speed

The difference between the pressure above (eq. S20) and below (eq. S27) the interface must be balanced by the capillary pressure (eq. S11),

$$\Delta p = p_0 - p^-(y=0) = (\alpha + i\beta)\rho U_1^2 \frac{k_x^2}{k}\eta - \rho\frac{k_x^2}{k}c^2\eta = \Delta p_{\text{cap}} = -\gamma k^2 \eta. \tag{S28}$$

Solving for c and including the expression for α_1,

$$2c^2 = \frac{\gamma}{\rho}\frac{k^3}{k_x^2} + (\alpha_2 + i\beta)U_1^2 \implies c = c_w\left(1 + \frac{1}{4}(\alpha_2 + i\beta)\frac{U_1^2}{c_w^2} + \dots\right), \tag{S29}$$

where $c_w = \sqrt{\dfrac{\gamma}{2\rho}\dfrac{k^3}{k_x^2}}$ is the unforced phase speed neglecting any contributions from α_2 and β and the dots denote higher order terms.

It is possible to find the k_x for which c_w assumes a minimum value by evaluating $\mathrm{d}c_w/\mathrm{d}k_x = 0$. The minimum value is, for $k_z = 2\pi/(2w)$,

$$c_{w,\min} = \sqrt{\frac{\gamma}{\rho}\frac{3^{3/2}}{4}k_z} = \sqrt{\frac{\gamma}{\rho}\frac{3^{3/2}}{4}\frac{\pi}{w}} \implies c^+_{w,\min} = \sqrt{\frac{1}{\mathrm{We}^+ w^+}\frac{3^{3/2}\pi}{4}} \approx \sqrt{\frac{\pi}{\mathrm{We}^+ w^+}}. \tag{S30}$$

E. Derivation of β

In this section, we find an expression for β. Returning to eq. (S18), dividing by $\tilde{u}$, multiplying by the complex conjugate of $\tilde{v}$, namely $\tilde{v}^*$, integrating from $\xi = \xi_0$ to $\xi = \infty$, integrating $\tilde{v}''\tilde{v}^*$ by parts, and using the boundary conditions above (eqs. S12 and S17),

$$\int_{\xi_0}^{\infty}\{|\tilde{v}'|^2 + [1 + \tilde{u}''/\tilde{u}]|\tilde{v}|^2\}\mathrm{d}\xi = [\tilde{v}^*\tilde{v}']_{\xi_0}^{\infty} = -\tilde{u}_0\tilde{v}_0'. \tag{S31}$$

Hence, the imaginary part of eq. (S21) is

$$\beta = \Im(\tilde{u}_0\tilde{v}_0') = -\Im\left(\int_{\xi_0}^{\infty}(\tilde{u}''/\tilde{u})|\tilde{v}|^2\mathrm{d}\xi\right). \tag{S32}$$

By calculus of residues [16], this expression can be evaluated to

$$\beta = -\pi|\tilde{v}_c|^2\frac{\tilde{u}_c''}{\tilde{u}_c'} = -\pi\left|\frac{v_c}{k_x\eta U_1}\right|^2\frac{1}{k}\frac{U_c''}{U_c'}, \tag{S33}$$

where the subscript c denotes values at the location where $\tilde{u} = 0$, $\xi = \xi_c$. To find an expression for $\tilde{v}_c$, eq. (S18) can be re-written as

$$(\tilde{u}\tilde{v}' - \tilde{u}'\tilde{v})' = \tilde{u}\tilde{v}. \tag{S34}$$

Integrating between $\xi = \xi_c$ and $\xi = \infty$ gives,

$$\tilde{v}_c = \frac{1}{\tilde{u}_c'}\int_{\xi_c}^{\infty}\tilde{u}\tilde{v}\mathrm{d}\xi. \tag{S35}$$

We now use the same approximate solution of $\tilde{v}$ as above. This approximation gives

$$\beta = -\pi\frac{\tilde{u}_c''}{\tilde{u}_c'^3}\left[\int_{\xi_c}^{\infty}e^{-\xi}\tilde{u}^2\mathrm{d}\xi\right]^2. \tag{S36}$$

The solution to the full equation has been given by Conte & Miles [17]. Assuming a logarithmic profile, $U = u_\tau/\kappa\log(y/z_0) \implies \tilde{u} = \log(\xi/\xi_c)$. We have here set the reference velocity, $U_1 = u_\tau/\kappa$, where κ is the von Kármán constant. With eq. (S36),

$$\beta = \pi\xi_c\left[\int_{\xi_c}^{\infty}e^{-\xi}\log(\xi/\xi_c)^2\mathrm{d}\xi\right]^2. \tag{S37}$$

F. Condition for wave growth

To the first order, the imaginary wave speed corresponds to

$$c_i = c_w \frac{1}{4} \beta \frac{U_1^2}{c_w^2}, \tag{S38}$$

giving wave growth when non-zero. The relation for β, eq. (S37), can be computed and is plotted in fig. S7. There is a sharp decrease in β at about $\xi_c \approx 1$. This means that in order to have amplitude growth,

$$\xi_c = k y_c \lesssim 1 \implies y_c \lesssim \frac{1}{k} < \frac{w}{\pi}, \tag{S39}$$

where we use the upper bound of $1/k$ as given by eq. (S24).

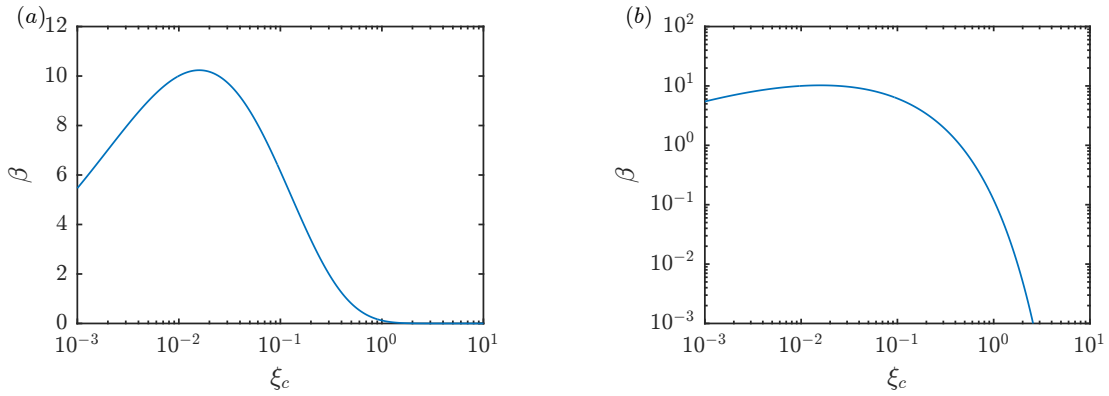

FIG. S7: Plot of β verses $\xi_c = k y_c$, with (a) linear and (b) logarithmic vertical axis.

S4. SPACE-TIME CORRELATIONS

Space-time correlations are shown in fig. S8 for $\mu_i/\mu_\infty = 1$ and We = 100 and 200.

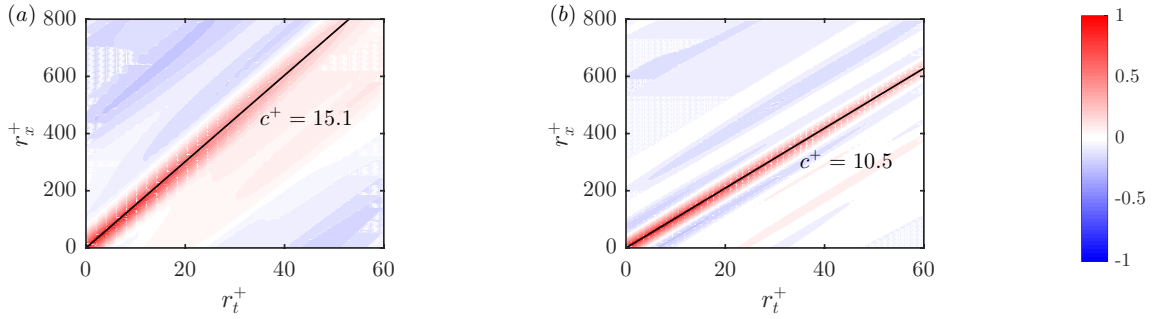

FIG. S8: Space-time correlation of interface height in the middle section of a groove, for $\mu_i/\mu_\infty = 1$ and (a) We = 100 and (b) We = 200. Streamwise displacement is denoted r_x^+ and time difference r_t^+. The slope of the region with highest correlation corresponds to the dominating phase speed, marked by a black line.

[1] P. Costa, "A fft-based finite-difference solver for massively-parallel direct numerical simulations of turbulent flows," *Comput. Math. with Appl.*, vol. 76, no. 8, pp. 1853–1862, 2018.

[2] W. P. Breugem and B. J. Boersma, "Direct numerical simulations of turbulent flow over a permeable wall using a direct and a continuum approach," *Phys. fluids*, vol. 17, no. 2, p. 025103, 2005.

[3] S. Afkhami and M. Bussmann, "Height functions for applying contact angles to 2d vof simulations," *Int. J. Numer. Methods Fluids*, vol. 57, no. 4, pp. 453–472, 2008.
[4] T. D. Blake, "The physics of moving wetting lines," *J. Colloid Interface Sci.*, vol. 299, no. 1, pp. 1–13, 2006.
[5] D. Legendre and M. Maglio, "Comparison between numerical models for the simulation of moving contact lines," *Comput. Fluids*, vol. 113, pp. 2–13, 2015.
[6] M. Lee and R. D. Moser, "Direct numerical simulation of turbulent channel flow up to $re_\tau \approx 5200$," *J. Fluid Mech.*, vol. 774, pp. 395–415, 2015.
[7] C. Schönecker, T. Baier, and S. Hardt, "Influence of the enclosed fluid on the flow over a microstructured surface in the cassie state," *J. Fluid Mech.*, vol. 740, pp. 168–195, 2014.
[8] M. K. Fu, I. Arenas, S. Leonardi, and M. Hultmark, "Liquid-infused surfaces as a passive method of turbulent drag reduction," *J. Fluid Mech.*, vol. 824, p. 688, 2017.
[9] Z. Ge, H. Holmgren, M. Kronbichler, L. Brandt, and G. Kreiss, "Effective slip over partially filled microcavities and its possible failure," *Phys. Rev. Fluids*, vol. 3, no. 5, p. 054201, 2018.
[10] R. G. Cox, "The dynamics of the spreading of liquids on a solid surface. part 1. viscous flow," *J. Fluid Mech.*, vol. 168, pp. 169–194, 1986.
[11] J. Jiménez, "Turbulent flows over rough walls," *Annu. Rev. Fluid Mech.*, vol. 36, pp. 173–196, 2004.
[12] P. Orlandi, S. Leonardi, R. Tuzi, and R. A. Antonia, "Direct numerical simulation of turbulent channel flow with wall velocity disturbances," *Phys. Fluids*, vol. 15, no. 12, pp. 3587–3601, 2003.
[13] P. Orlandi and S. Leonardi, "Dns of turbulent channel flows with two-and three-dimensional roughness," *J. Turbul.*, vol. 7, p. N73, 2006.
[14] P. J. Schmid and D. S. Henningson, *Stability and transition in shear flows*, vol. 142. Springer Science & Business Media, 2012.
[15] D. J. Acheson, "Elementary fluid dynamics," 1991.
[16] J. W. Miles, "On the generation of surface waves by shear flows," *J. Fluid Mech.*, vol. 3, no. 2, pp. 185–204, 1957.
[17] S. D. Conte and J. W. Miles, "On the numerical integration of the Orr-Sommerfeld equation," *J. Soc. Ind. Appl. Math.*, vol. 7, no. 4, pp. 361–366, 1959.